Increased flow rate of hyperpolarized aqueous solution for DNP-enhanced MRI achieved by an open Fabry-Pérot type microwave resonator

Alexey Fedotov[1], Ilya Kurakin[1], Sebastian Fischer[2], Thomas Vogl[2], Thomas F. Prisner[3], Vasyl Denysenkov[3]

[1] Institute of Applied Physics of the Russian Academy of Sciences, Nizhny Novgorod, 603950, Russia

[2] Institute of Diagnostic and Interventional Radiology, University Hospital Frankfurt, Frankfurt am Main, 60590, Germany

[3] Institute of Physical and Theoretical Chemistry and Center of Biomolecular Magnetic Resonance, Goethe University, Frankfurt am Main, 60438, Germany

Correspondence to:

Thomas F. Prisner (Prisner@chemie.uni-frankfurt.de) and Vasyl Denysenkov (Denysenkov@em.uni-frankfurt.de)

Abstract. A continuous flow dynamic nuclear polarization (DNP) employing the Overhauser effect at ambient temperatures can be used among other methods to increase sensitivity of magnetic resonance imaging (MRI). The hyperpolarized state of water protons can be achieved by flowing aqueous liquid through a microwave resonator placed directly in the bore of a 1.5 T MRI magnet. Here we describe a new open Fabry-Pérot resonator as DNP polarizer, which exhibits a larger microwave exposure volume for the flowing liquid in comparison with a cylindrical TE_{013} microwave cavity. The Fabry-Pérot resonator geometry was designed using quasi-optical theory and simulated by CST software. Performance of the new polarizer was tested by MRI DNP experiments on a TEMPOL aqueous solution using a blood-vessel phantom. The Fabry-Pérot resonator revealed a 2-fold larger DNP enhancement with a 4-fold increased flow rate compared to the cylindrical microwave resonator. This increased yield of hyperpolarized liquid allows MRI applications on larger target objects.

1 Introduction

Magnetic resonance imaging is a widespread method in clinical diagnostics providing *in vivo* information on physiological and metabolic changes in tissue. MRI is a non-invasive method because of the low excitation frequency in the radiofrequency range. However, this implies also the low sensitivity of the method, leading to long acquisition times. This can be improved by moving to higher magnetic fields, but on the cost of high prices and large technical demands. Contrast between different tissues is another concern. Contrast agents, as for example Gd-complexes are typically used to improve the contrast. However, in few cases, it induces side effects like allergic reactions and nephrogenic systemic fibrosis (Perazella, 2009, Thomsen, 2008, Kuo et al., 2007). Besides, potential long-term implications arising from the permanent deposition of the Gd-complexes in the

brain are currently under discussion (Semelka et al., 2016, Topcuoglu et al., 2020). As an alternative, hyperpolarization methods have been explored to improve sensitivity and contrast for MRI applications. Different strategies have been used so far to hyperpolarize an agent for MRI applications. Optical polarized noble gases as well as para-hydrogen have been used as
35   hyperpolarized molecules for MRI (Salerno et al., 2001, Albert and Balamore, 1998, Limburn et al., 2013, Golman et al., 2001, Duckett and Mewis, 2012, Cavallari et al., 2018). Another method is DNP (dynamic nuclear polarization) where unpaired electron spins excited by microwaves are used to hyperpolarize nuclear spins. Initially this method has been used either at very low magnetic fields or with rapid field cycling (Foster et al., 1998) because microwave radiation cannot penetrate deep into living tissue, or later by hyperpolarizing molecules externally before injection.

40   Dissolution DNP is a commercially available hyperpolarization method of liquid substrates for MRI (Olsson et al., 2006). It uses metabolites such as ^{13}C-pyruvate, which are polarized externally to the MRI magnet at very low temperatures (~1 K) by the solid effect. Within 5 minutes a polarization of 10% can be achieved (Bornet and Jannin, 2016). After the hyperpolarization procedure is complete, the frozen substrate is rapidly transported to the imager magnet, dissolved in hot liquid, and injected into the body. The typical (dissolving and transfer) time of 5–15 seconds limits the *in vivo* usage to ^{13}C and ^{15}N. It is difficult
45   to detect hyperpolarized protons with this approach because of the short relaxation time of water protons compared to the transfer time (Ardenkjaer-Larsen et al., 2014). Therefore, the method is mostly used for the study of cellular metabolism with pyruvate, lactate or other metabolic precursors labelled with low-gyromagnetic ratio nuclei having long relaxation times (Mishkovsky et al., 2012, Jannin et al., 2019). The observation time window is limited by the relaxation time of the hyperpolarized nuclei. Long-lived singlet states might allow to extend this time window (Pileio et al., 2006, Dumez et al.,
50   2017).

Hyperpolarization by the Overhauser mechanism is well suited for physiological solutions under continuous flow conditions, because of the rapid polarization transfer from the unpaired electrons of the radicals to proton spins of the solvent. The polarization transfer in liquids works most efficiently at low magnetic fields. Therefore, first Overhauser DNP experiments for MRI (Guiberteau and Grucker, 1997, Krishna et al., 2002), and proton-electron double-resonance imaging (PEDRI) (Foster et
55   al., 1998) were demonstrated at low magnetic fields of 6–15 mT. This allows irradiation of the paramagnetic radical inside the mouse or rat body in the MRI magnet. Such experiments, however, cannot be performed in clinical MRI scanners at higher magnetic fields (respectively at higher frequencies) due to the strong absorption of microwaves in living tissues, resulting in unwanted heating. A second approach is again to hyperpolarize molecules outside of the target object. This can be done by placing a mw resonator with the radicals into the fringe field of the MRI magnet (Lingwood et al., 2012) or directly inside the
60   MRI magnet close to the target object (Krummenacker et al., 2012). In the first case the hyperpolarization step is done at a lower magnetic field compared to the MRI detection field. This gives a higher polarization transfer efficiency, because the Overhauser effect in liquids is optimal at low magnetic fields. However, the maximal enhancement achieved at the imaging object is downscaled by the ratio between the polarizing and the imaging detection field. For example, in case of an X-band polarizer operating at $B_0 = 0.3$ T and a 1.5 T MRI scanner this reduction factor is 5-fold.

65

In our "in-bore" 1.5 T MRI DNP setup there is no such 'Boltzmann factor penalty' and a water proton signal enhancement of up to 100 has been reached under static conditions (Krummenacker et al., 2012). On the other hand, the dimensions of fundamental resonators scale down inversely with the mw frequency. Technical challenges are due to the unavoidable high dielectric losses of water in the mw frequency range (Neumann, 1985). These dielectric losses of aqueous samples result in a

70 decrease of the resonators Q-factor, and strong heating of the liquid. The heating can be minimized by applying a resonance mw structure with well separated E and B components of the applied mw field and by placing the sample in a node of the E component. Therefore, cross-section dimensions of the liquid sample inside the resonator have to be much smaller than the mw wavelength. This leads also to very short retention times in case of the flowing liquid. The attainable yield is defined by the highest possible flow rate at a maximum DNP enhancement in such non-stop-flow polarizers. It depends on: 1) - the dwell

75 time of water molecules inside the mw polarizer, which should be longer than the proton relaxation time for an optimal DNP build-up, and 2) - the mw B_1 field strength, which defines the efficiency of saturation of the EPR transitions of the dissolved TEMPOL radicals. The B_1 value at the sample depends on the conversion factor c and the quality factor Q of the mw resonance structure, and the applied mw power P_{mw} (Eq. 1) (Poole, 1967, Rinard and Eaton, 2005).

$$B_1 = c\sqrt{Q \cdot P_{mw}} \qquad (1)$$

80 The quality factor Q of the resonator itself depends on the geometry of the mw resonance structure and on sample properties, such as size of the sample and its dielectric constant ε_r.

Conveniently, cylindrical capillaries made of quartz can be used as liquid sample holders. For this reason, the natural choice of the mw resonator geometry is also cylindrical geometry, such as TE_{01n} type cavities. Such resonators have high Q factors as well as high conversion factors c for frozen solution samples and are commonly used in EPR spectroscopy (for instance, Q

85 = 4000 for an unloaded TE_{012} resonator at 95 GHz mw frequency has been reported (Smirnov and Smirnova, 2001). This leads to a large B_1 field strength, which is advantageous for pulsed EPR applications. The situation is quite different for MRI DNP applications. Here the aqueous sample is in the liquid state, strongly increasing the mw absorption if the sample capillary diameter is not strongly reduced. On the other hand, larger amounts of hyperpolarized liquids are preferable to be able to enhance contrast of as large as possible objects under MRI study.

90 Fabry-Pérot resonators are mw resonance structures suitable for larger sample volumes, because different from fundamental mode mw cavities, the sample size is only limited in one dimension (direction of the mw excitation) much less than wavelength to avoid absorption of the E field component (Budil and Earle, 2004). Among known quasi-optical mw resonators (Lynch et al., 1988, Prisner et al., 1992, Barnes and Freed, 1997, Milikisiyants et al., 2018, Blok et al., 2004, van Tol et al., 2005, Neugebauer and Barra, 2010) a semi-confocal Fabry-Pérot resonator with the sample placed on the surface of a massive metal

95 (copper) block acting as the plain mirror can best satisfy heat dissipation conditions (Denysenkov and Prisner, 2012).

Here we report on such a new open resonator for Overhauser DNP applications within a whole-body 1.5 T MRI scanner. Particular effort was directed at reaching a uniform (plateau like) microwave field distribution along the flow direction to obtain an efficient polarization transfer to water molecules in the polarizer. The performance of the "in-bore" MRI DNP

polarizer equipped with the new resonator was tested and compared to the cylindrical TE$_{013}$ cavity described before

100 (Denysenkov et al., 2017).

2 Methods and Materials

2.1 Design and simulation of the resonator

An increase of the flow rate for a constant residence time of water molecules inside the mw cavity requires a corresponding

105 increase of the cavity dimensions in flow direction. This can result in a higher spectral density of mw modes of the cavity, which could prevent the selective excitation of the desired mode. Excitation of other modes with similar frequency would distort the standing mw field pattern inside the cavity and thus reduce the excitation efficiency. In contrast, the use of a Fabry-Pérot open resonance structure avoids such problems. Moreover, the semi-confocal arrangement, where the thin layer liquid sample is directly placed on top of the flat copper mirror, allows effective cooling. A schematic drawing of the new Fabry-

110 Pérot resonator for DNP is depicted in Figure 1.
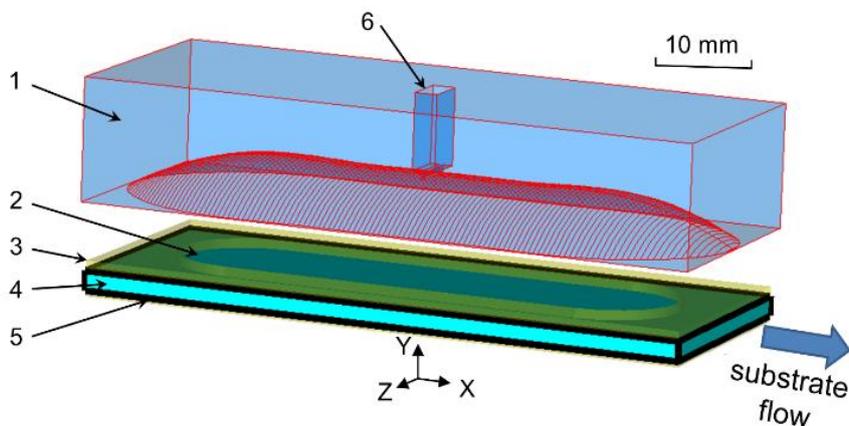
Figure 1: Design of open mw resonance structure for MRI DNP. 1- concave mirror (copper), 2- aqueous sample, 3- fixture (brass), 4- cover plate (sapphire), 5- plain mirror (copper), 6- waveguide port. Aqueous solution flow direction is indicated by the "substrate flow" arrow.

115

Typically, Fabry-Pérot resonators use concave mirrors of elliptical or parabolic geometry. These mirrors provide Gaussian (or quasi-Gaussian) transverse distribution of the microwave field intensity at the mirror surface. However, for the considered DNP application a uniform distribution of the B_1 field along the flow direction is preferable. It facilitates the polarization transfer from the unpaired electron spin of the TEMPOL radical to the proton spin of the water molecules, within their residence

120 time inside the resonance structure. Therefore, the shape of the concave top mirror was calculated using an inverse design procedure, as described before (Belousov et al., 2000). In this approach, the B_1 field distribution at the flat mirror is assumed as quasi-homogeneous with the same phase. With this boundary condition, the field propagation inside the resonator is calculated.

The concave mirror shape is found as a surface where the phase of the calculated field is equal to $q\pi$, were q is an integer (in our case, $q = 4$, so that we use the 4th axial mode of the cavity). In these simulations the exact equations of the microwave field propagation are used instead of the paraxial approximation for higher accuracy. The possible influence of the finite sizes of both the flat and the concave mirrors was analyzed by an iterative method after the mirror shape was fixed (Fox and Li, 1961). For this purpose, the microwave field propagation from one mirror to the other one was iteratively calculated. For each passage, the phase of the microwave field components was inverted at the mirror surfaces, while the mw power traveling outside of the mirror surfaces was assumed as the power lost. This procedure provides easily the first eigenmode of the resonator with the highest Q factor. The eigenfrequency of this mode is found by satisfying the standing wave condition that the phase change along the wave round-trip in the cavity is equal to $2\pi q$. The quality factor Q of the empty resonance structure can be determined by the mw losses per cycle due to finite mirror sizes. The simulations show that the influence of the finite mirror size are much less than the power loss arising from the liquid sample and therefore negligible. The obtained B_1 field distribution at the surface of the flat mirror and the calculated shape of the concave mirror are shown in Figure 2.
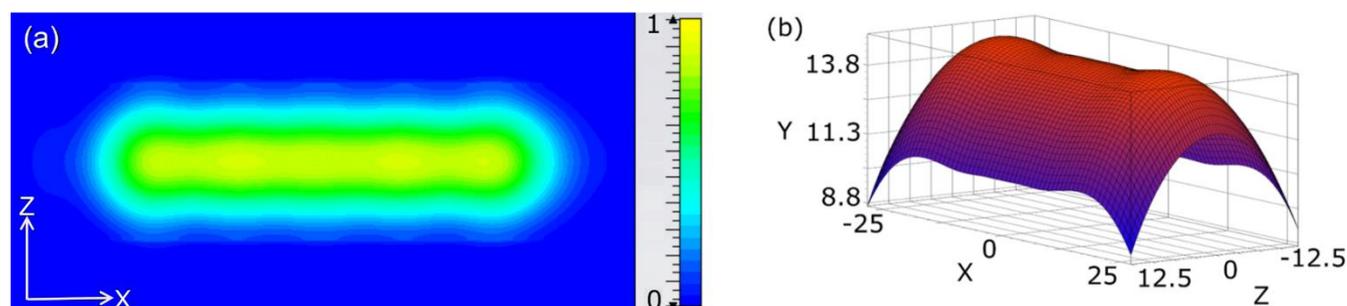
Figure 2: Microwave magnetic field distribution in open resonator. a) The simulated microwave magnetic field distribution (normalized) at the plain mirror. The substrate flow is along the horizontal X direction. b) The calculated shape of the concave mirror (scale is in mm).

The obtained concave mirror profile has been used further for the open resonator simulation by using CST STUDIO SUITE (Darmstadt, Germany). These simulations take into account the microwave losses in the aqueous sample and the influence of the coupling slit between the cavity and feeding waveguide. The simulated geometry is shown in Figure 1 with a 80 μm thick water layer on top of the plain mirror covered by a sapphire plate (1.5 mm), thick enough to withstand the pressure applied under flow conditions (up to 7 bar). The dielectric permittivity of pure water with a temperature close to 100 °C at 42 GHz was set to $\varepsilon' = 47$, $\varepsilon'' = 32$ (loss tangent $\tan\delta = 0.68$) (Andryievski et al., 2015). The resonance modes (TEM_{00}, TEM_{02}, TEM_{04}) of the resonator with the respective B_1 distribution along the water layer are shown in Figure 3.
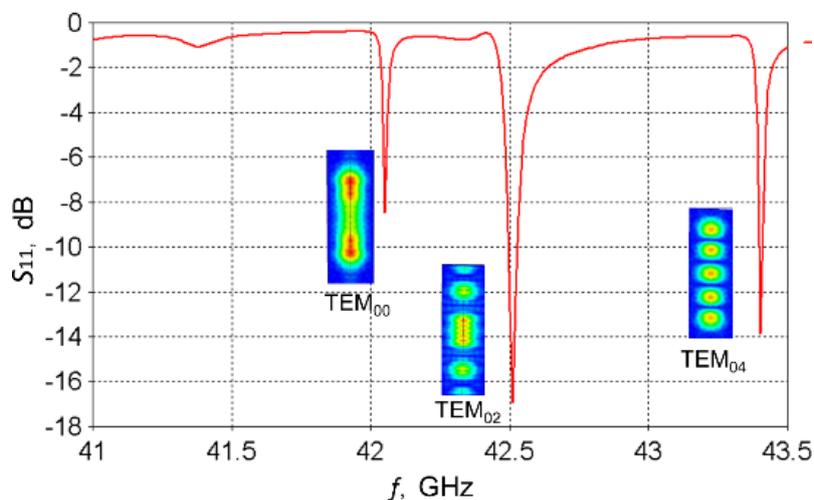
150 **Figure 3:** The simulated modes of the open resonator. The corresponding resonance modes are identified by calculation of the B_1 field distribution at the plain mirror (shown as insets).

In the simulations, the slit width between the feeding waveguide and the cavity was optimized to achieve the most effective mw excitation. Since the mw absorbance in the water layer is strong, a slit dimension as large as 1.4x5.6 mm^2 is needed to
155 reach the critical coupling. Therefore, the wave scattering by the coupling slit results in some distortion of the B_1 field homogeneity at the flat mirror (Figure 4a). The simulation predicts a Q factor of the TEM$_{00}$ mode of the resonator of 800 and a maximal conversion factor c of about 3 G/W ^{½}. Uniformity of the RF magnetic field over the sample volume is also an important parameter beside the B_{1max} value (Mett et al., 2019) that can be evaluated by calculating the mean value of B_1. In the Fabry-Pérot resonator the B_1 mean value over the sample volume is about 1.55 G/W ^{½} that is slightly higher in comparison to
160 the TE$_{013}$ cylindrical cavity (1.4 G/W ^{½}) (Figure 4b) used in our MRI DNP experiments previously (Denysenkov et al., 2017). The simulations show that the effectively irradiated area on the plain mirror surface is about 40x12 mm^2, corresponding to 40 μl volume of aqueous solution inside the resonator for an 80 μm thick layer.

165   a)   b)
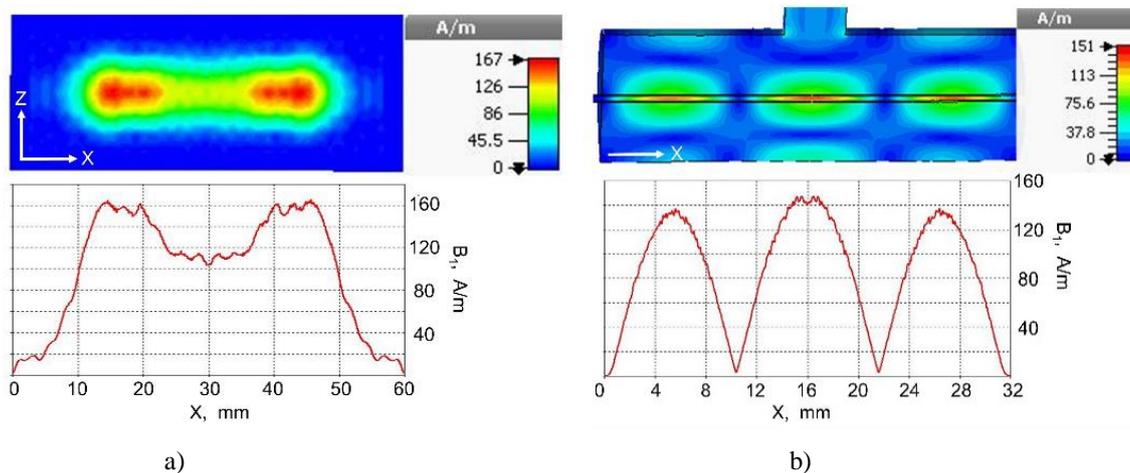
Figure 4: Comparison of field distribution of open resonator with cylindrical resonator. (a) Calculated B_1 field distribution at the plain mirror surface of the Fabry-Pérot resonator in presence of an aqueous layer of 80 μm for the TEM_{00} mode; (b) B_1 distribution along the 0.5 mm ID quartz capillary with water along the TE_{013} cylindrical cavity. The B_1 value is calculated for an input mw power of 0.5 W.

170   2.2 MRI DNP setup

MRI detection was performed by a 1.5 T MRI scanner (Magnetom Aera, Siemens, Erlangen, Germany) using a standard 8-channel surface pick-up coil (NORAS, Germany) positioned horizontally in the iso-center of the magnet bore (Figure 5).

175

Figure 5: In-bore Overhauser DNP-MRI setup. 1- mw resonator, 2- waveguide between the mw resonator and the microwave board, 3- syringe pump, 4- microwave board.

According to the "in-bore" concept, the polarization transfer from the TEMPOL radical electron spins to the water protons as

180   well as the MRI detection are accomplished at ambient temperature in the same 1.5 T magnetic field. This corresponds to an

EPR excitation frequency of 42 GHz [Denysenkov et al., 2017].

All MRI images were taken on a meander-shaped phantom made of a 0.4 mm ID and 300 mm long PTFE tubing shown in

Figure 6, in which the hyperpolarized solution from the resonator was transferred via a piece of 0.25 mm ID quartz capillary

(Polymicro Technologies, USA). The phantom was placed directly on top of the pick-up coil for optimal sensitivity. For

185   imaging the standard 2D slice-selective gradient echo (GRE) experiment with Cartesian k-space filling was used with the

number of encoding steps of 144, a repetition time (TR) of 110 ms, an echo time (TE) of 3.8 ms, a pixel bandwidth of 310 Hz,

an acquisition matrix of 192x256 and a field-of-view (FOV) of 90x120 mm^2. The slice thickness was chosen in a range of 3

mm to minimize TE and signal-to-noise losses due to flow induced dephasing. The excitation RF pulse flip angle (FA) was set

to 65° to meet the optimal conditions for the best signal contrast and sensitivity. The signal-to-noise-ratio (SNR) of the

190   reference image (without DNP) was improved by acquiring 3 averages per scan resulting in an overall duration of 47 sec. The

SNR was determined by measuring the maximal signal intensity at the inlet area of the phantom and the standard deviation of

the noise outside the phantom.
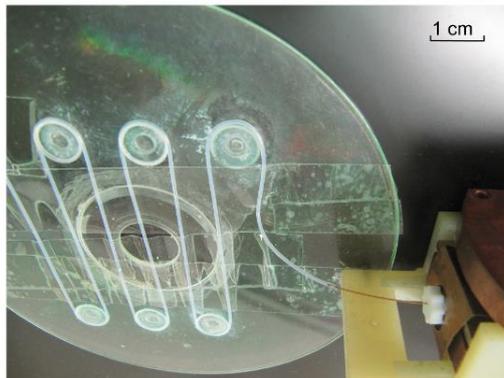
Figure 6: Phantom used for the DNP-MRI measurements. The meander-shaped 0.4 mm ID PTFE tubing is mimicking a blood vessel. Inlet

195   of the phantom is connected to the resonator via a piece of 0.25 mm ID quartz capillary (right-bottom corner of the picture).

The nitroxide radical TEMPOL (4-hydroxy-2,2,6,6-tetramethylpiperidine-1-oxyl, Sigma-Aldrich, USA) was used as DNP

agent to polarize water protons. The concentration of the radical was 28 mM. Measurements of DNP enhancements and SNR

were done for flow rates of the TEMPOL aqueous solution ranging from 0.5 to 4 ml/min. Such flow rates of the aqueous

200   solution have been accomplished by using a 10 ml syringe driven by an ALADDIN syringe pump (WPI Inc., USA), and

injected into the resonator via a 0.8 mm ID PTFE tube.

3   Experimental Results

3.1 Resonator performance

205   The open resonator (Figure 7) was home-build in the workshop of the Institute of Physical and Theoretical Chemistry at the Goethe University Frankfurt and tested experimentally for its mw performance with a Rohde & Schwarz ZVA-40 network analyzer (Munich, Germany).
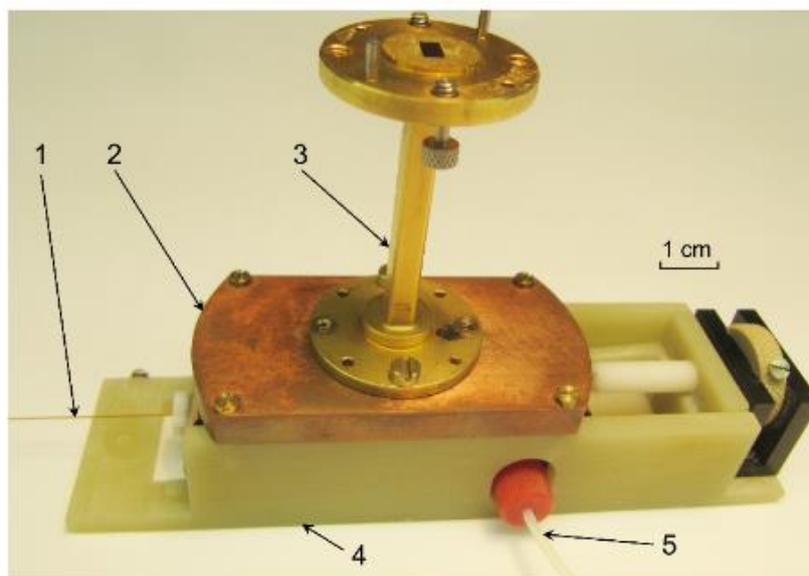
210   **Figure 7:** The resonator assembly. 1 - quartz capillary from the resonator to phantom, 2 - concave mirror, 3 - WR-22 waveguide, 4 - housing including the plain mirror, 5 - 0.8 mm ID tubing from the syringe filled with the TEMPOL solution.

The measured frequency response showed several resonance modes (Figure 8) which can be identified according to the resonance frequencies calculated previously by CST (compare with Figure 3).

215
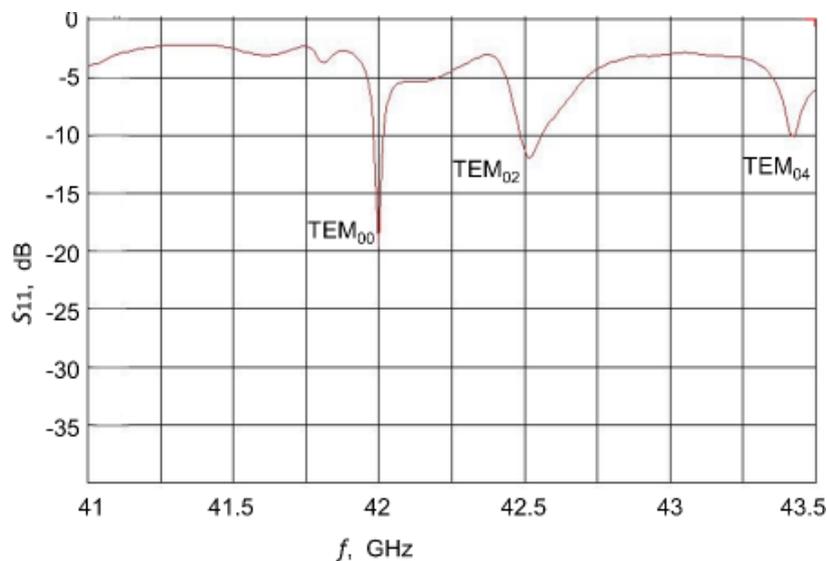
Figure 8: Experimental frequency response of the open resonator. The water layer is 50 μm thick, the sapphire window is 1.5 mm thick, and the separation between mirrors is 2λ. The different resonance dips are identified by comparison with the CST simulations shown in Figure 3.

220

The TEM_{00n} mode was chosen for the DNP experiments due to its high homogeneity of the B_1 field distribution along the flow axis and the highest average value of B_1 over the sample. The longitudinal mode number n defines the number of $\lambda/2$ wavelengths between the two mirrors. It was set to $n = 4$ for our experiments to reach a critical mw coupling to the resonator and avoid any reflection losses. The measured Q value of this resonance mode is about 700 when the resonator is filled with a

225 50 μm thick water layer on top of the plain mirror. It resulted in the conversion factor of 1.55 $G/W^{1/2}$ (mean value) over the sample volume, which agreed very with the value calculated by the CST software. This demonstrates that finite element calculations are as good as measurements in a well-characterized resonator (Rinard and Eaton, 2005).

3.2 MRI DNP Results

230

MRI images of the TEMPOL/water solution flowing through the meander-shaped phantom were taken to investigate the DNP performance with the new setup. Figure 9 shows the images taken with a GRE sequence with the parameters described before. The substrate flows from the right side to the left side. The image of the radical solution without mw irradiation in the resonator is shown in Figure 9a. In this case, 3 acquisitions were necessary to get an appropriate SNR. The water signal at the inlet is

235 weaker because the first loop of the tubing moves out of the phantom plane and therefore leaves the MRI slice (see Figure 6). The image on the right side (Figure 9b) was obtained as a single acquisition with the microwaves turned on to its maximum power of 10 W at the microwave board. Both pictures are taken with the same flow rate of 2.5 ml/min. The signal intensity

under DNP conditions at the inlet is 18-fold larger compared to the control experiment without mw irradiation. As can be seen from the picture the enhancement fades away along the pathway of the flowing liquid and disappears at approximately 22 cm.

240
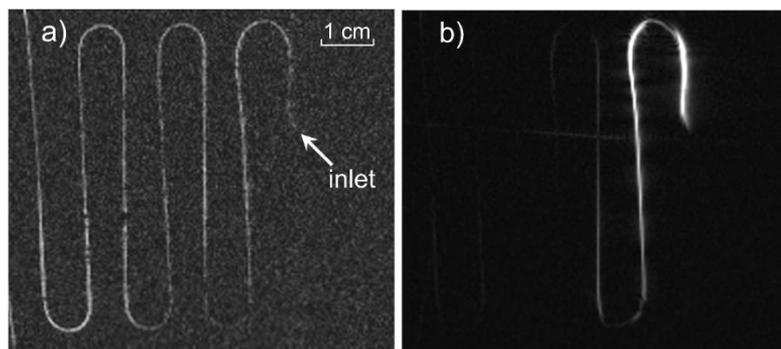
Figure 9: MRI image of TEMPOL aqueous solution flowing through the phantom. a) Without microwaves, 3 acquisitions; b) with microwaves, single acquisition. Phantom inlet position is indicated by the arrow. The radical concentration is 28 mM and the flow rate is 2.5 ml/min.

245

MRI images were taken also at different flow rates to quantify the superior performance of the new open resonator (with the TEM_{004} mode) compared to the cylindrical TE_{013} cavity. The signal enhancement (ratio of signal with and without mw) at the inlet versus different flow rates for both resonators is shown in Figure 10. As can be seen the signal enhancement is a factor of 2 larger with the Fabry-Pérot resonator compared to the cylindrical one. The maximum enhancement of 18 is reached for a

250 flow rate of 2.5 ml/min.
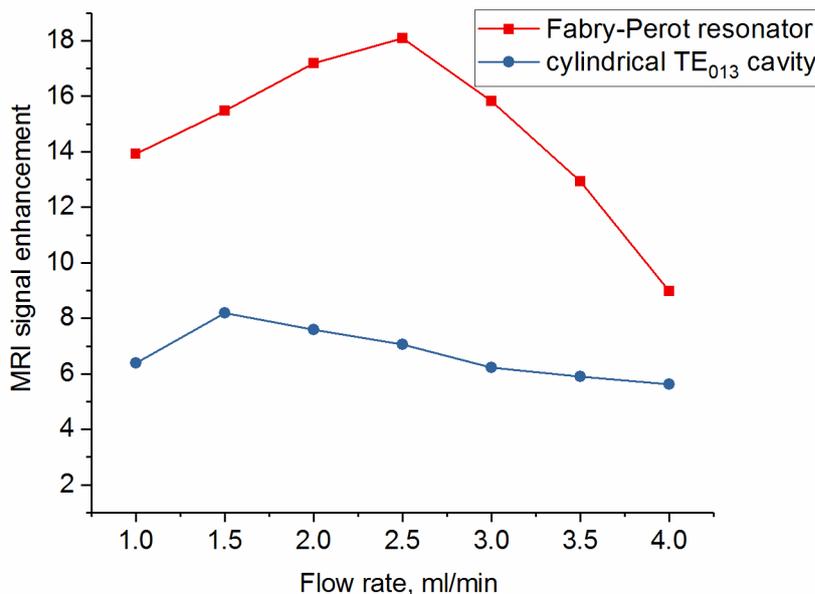
Figure 10: DNP MRI signal enhancements as a function of the flow rate. Shown are the results with the new Fabry-Pérot resonator (red) and the cylindrical cavity (blue) at a mw power of 10 W.

255

4 Discussion

The experimental tests showed that the new resonator has a good mw performance only if the thickness of the water layer is reduced to 50 μm with respect to the value of 80 μm used in the CST simulations. This can be explained by imperfections of

260 the real device geometry caused by fabrication steps, as well as by the higher mw losses (tanδ =1.2) in the water sample at room temperature (Ellison et al., 1996), which was the experimental temperature at the mw characterization of the device with a network analyser with low amount of mw output power (no heating). In the DNP experiments the temperature of the sample is between 65 °C and 95 °C due to the heating by the much higher applied mw power of 10 W. The higher temperature of the water solution in the DNP resonator shortens the rotational and translational correlations times improving the maximum

265 achievable signal enhancements. After leaving the mw resonator the temperature of the hyperpolarized solution in the outlet capillary can be brought back to any desired temperature by a heat-sink chiller as described before (Denysenkov et al., 2017) to be physiologically compatible with *in vivo* experiments.

The optimum flow rate for signal enhancement by DNP is a trade-off between the dwell time of the liquid inside the mw resonator and the flow time through the phantom. The first aspect requires low flow rates to achieve maximum polarization

270 build-up, which is on the timescale of the proton spin relaxation time T_1. The second aspect requires high flow rates to reduce

the hyperpolarization losses due to proton T_1 relaxation determined by the flow time through the phantom. As a consequence of this second point, the highest enhancement is observed at the inlet of the phantom due to the shortest time delay after the DNP polarization process inside the resonator.

The DNP enhancement observed at this point is more than a factor of 2 larger for the new open Fabry-Pérot resonance structure
275 compared to the cylindrical cavity (Figure 10). The reason is the much larger sample volume inside of the new resonator (25 μl) compared to the cylindrical cavity (6.3 μl), leading to a much longer residence time of the liquid under flow conditions and therefore a larger starting polarization. The achieved B_1 field strength with the Fabry-Pérot resonator is only 10% smaller compared to the cylindrical cavity for the TE_{013} mode. This is due to the fact that a higher Q values can be achieved with the new resonance structure by minimizing the electrical field component of the mw at the sample along the full pathway within
280 the resonator. This cannot be fulfilled as well for the higher mode cylindrical cavity. Similarly, the B_1 field in the new resonator is much more homogeneous along the pathway of the sample compared to the cylindrical cavity. All these factors lead to an expected larger DNP enhancement of the liquid at the exit of the new resonator.

The hyperpolarization of the liquid relaxes exponentially back to the thermal Boltzmann equilibrium polarization after leaving the DNP resonator with a time constant given by the proton T_1 relaxation time. For the 28 mM TEMPOL solution this time is
285 approximately 0.17 s. Depending on the flow characteristics (laminar, bolus or turbulent) this would lead to a decrease of the polarization of 1/e after approximately 10-15 cm path length inside of the phantom. The experimentally observed decay is much faster due to the chosen gradient echo pulse sequence with a short TR of 110 ms. This time is much shorter than the travel time of the hyperpolarized liquid within the meander-shaped pathway of the phantom. Therefore the hyperpolarized liquid is excited several times by the RF π/2 pulse of the gradient echo sequence. Under our experimental conditions (flip
290 angle of 65°) each subsequent pulse reduces the hyperpolarization more than a factor of 2. This can be avoided by applying fast imaging techniques as echo planar imaging (EPI or SE-EPI), or/and SPatio-temporal ENcoding (SPEN) sequences that are single RF pulse experiments, instead of the multi-pulse GRE protocol used here. However, these sequences are technically more demanding and have to be optimized with respect to contrast and flow artefacts. The image of the DNP enhanced (bright) signal along the phantom tubing has some dark regions at the positions where the tubing is bent (see Figure 9b). This feature
295 can originate from some turbulence of the flow at these positions, leading to intra-voxel dephasing, which depends on the degree of turbulence and the direction of the phase- and frequency-encoding gradients with respect to the flow direction (Westbrook et al., 2011). To avoid these additional complications, we compare here the maximum achievable DNP polarization at the inlet point (approximately 5 cm after the resonator). With the new type of resonator not only larger enhancements but also a maximum at larger flow rates was achieved. This is again due to the larger sample volume inside the resonator. Therefore
300 larger amounts and stronger hyperpolarized liquids can be achieved with the new resonator type.

5 Conclusions

305

The developed open Fabry-Pérot resonator for Overhauser DNP exhibits an enlarged aqueous samples volume of 24 µl inside the mw resonator, a 4-fold increase with respect to a cylindrical TE_{013} cavity at 42 GHz. Additionally, the new resonator has a more homogeneous amplitude of the mw B_1 field along the sample pathway inside the resonance structure. The design of the resonator and sample geometry also leads to a reduced E_1 mw electrical field component along the sample pathway. This leads

310 to a larger Q value of 700 and thus to a similar efficient B_1 field amplitude (110 A/m) at the sample compared to a cylindrical TE_{013} cavity. First MRI DNP experiments with the new resonator demonstrate the possibility to increase the flow rate of hyperpolarized solutions significantly (4-fold) as well as to reach higher DNP enhancements (2-fold). This new resonance structure will be useful to improve Overhauser DNP MRI for angiography applications in the future.

315 *Author contributions.* AF simulated the resonator structure and wrote chapter 2 of the manuscript. IK calculated the concave mirror profile. SF optimized MRI protocol and wrote chapter 3 of the manuscript. TV supervised MRI experiments. TP supervised DNP supervision and wrote chapter 1 and 4 of the manuscript. VD planed the resonator improvements, designed the device, accomplished the resonator performance tests and participated in the MRI experiments. He also wrote the final version of the manuscript. All authors read and approved the final manuscript.

320 *Competing interests.* The authors declare no competing interests.

Acknowledgments. We acknowledge support by the Deutsche Forschungsgemeinschaft (DFG, German Research Foundation) and by the Center of Biomolecular Magnetic Resonance (BMRZ).

References

325 Albert, M. S., and Balamore, D.: Development of hyperpolarized noble gas MRI, Nucl. Instrum. Meth. Phys. Res., A402, 441–453, doi.org/10.1016/S0168-9002(97)00888-7, 1998.

Andryieuski, A., Kuznetsova, S. M., Zhukovsky, S. V., Kivshar, Y. S., and Lavrinenko, A. V.: Water: promising opportunities for tunable all-dielectric electromagnetic metamaterials, Sci. Rep., 5, 13535, doi.org/10.1038/srep13535, 2015.

Ardenkjaer-Larsen, J. H., Laustsen, C., Bowen, S., and Rizi, R.: Hyperpolarized H_2O angiography, Magn. Reson. Med., 71, 330 50–56, doi.org/10.1002/mrm.25033, 2014.

Barnes, J. P., and Freed, J. H.: Aqueous sample holders for high-frequency electron spin resonance, Rev. Sci. Instrum., 68, 2838–2846, doi.org/10.1063/1.1148205, 1997.

Belousov, V., Denisov, G., and Chirkov, A.: Calculation and parameter-control methods of eigenmodes of the simplest two-mirror resonators, Izv. Vuzov, Radiophys., 8, 738-746, doi.org/10.1023/A:1004869622320, 2000.

335 Blok, H., Disselhorst, J., Orlinskii, S. B., and Schmidt, J.: A continuous-wave and pulsed electron spin resonance spectrometer operating at 275 GHz, J. Magn. Reson., 166, 92–99, doi.org/10.1016/j.jmr.2003.10.011, 2004.

Bornet, A., and Jannin, S.: Optimizing dissolution dynamic nuclear polarization, J. Magn. Reson., 264, 13–21, doi.org/10.1016/j.jmr.2015.12.007, 2016.

Budil, D. E., and Earle, K. A.: Sample resonators for quasioptical EPR, in: O.Y. Grinberg, L.J. Berliner (Eds.), Very High

340 Frequency ESR/EPR, Springer, Boston, 2004.

Cavallari, E., Carrera, C., Sorge, M., Bonne, G., Muchir, A., Aime, S., and Reineri, F.: The ^{13}C hyperpolarized pyruvate generated by ParaHydrogen detects the response of the heart to altered metabolism in real time, Sci. Rep. 8, 8366, doi.org/10.1038/s41598-018-26583-2, 2018.

Denysenkov, V. and Prisner, T. F.: Liquid state dynamic nuclear polarization probe with Fabry-Perot resonator at 9.2 T, J.

345 Magn. Reson., 217, 1-5, doi.org/10.1016/j.jmr.2012.01.014, 2012.

Denysenkov, V., Terekhov, M., Maeder, R., Fischer, S., Zangos, S., Vogl, T., and Prisner, T.: Continuous-flow DNP polarizer for MRI applications at 1.5 T, Sci. Rep. 7, 44010, doi.org/10.1038/srep44010, 2017.

Duckett, S. B. and Mewis, R. E.: Application of parahydrogen induced polarization techniques in NMR spectroscopy and imaging, Acc. Chem. Res. 45, 1247–1257, doi.org/10.1021/ar2003094, 2012.

350 Dumez, J., Vuichoud, B., Mammoli, D., Bornet, A., Pinon, A., Stevanato, G., Meier, B., Bodenhausen, G., Jannin, S., and Levitt, M.: Dynamic Nuclear Polarization of Long-Lived Nuclear Spin States in Methyl Groups, J. Phys. Chem. Lett., 8, 3549-3555, doi.org/10.1021/acs.jpclett.7b01512, 2017.

Ellison, W. J., Lamkaouchi, K., and Moreau, J. M.: Water: a dielectric reference, J. Mol. Liq., 68, 171–279, doi.org/10.1016/0167-7322(96)00926-9, 1996.

355 Foster, M. A., Seimenis, I., and Lurie, D. J.: The application of PEDRI to the study of free radicals *in vivo*, Phys. Med. Biol., 43, 1893–1897, doi.org/10.1088/0031-9155/43/7/010, 1998.

Fox, A. G. and Li, T.: Resonant modes in a maser interferometer, Bell Labs Techn. J., 40, 453-488, doi.org/10.1002/j.1538-7305.1961.tb01625.x, 1961.

Golman, K., Axelsson, O., Johannesson, H., Mansson, S., Olofsson, C., and Petersson, J. S.: Parahydrogen-induced

360 polarization in imaging: Subsecond C-13 angiography, Magn. Reson. Med., 46, 1–5, doi.org/10.1002/mrm.1152, 2001.

Guiberteau, T. and Grucker, D.: Dynamic nuclear polarization imaging in very low magnetic fields as a noninvasive technique for oximetry, J. Magn. Reson., 124, 263–266, doi.org/10.1006/jmre.1996.1055, 1997.

Jannin, S., Dumez, J.-N., Giraudeau, P., and Kurzbach, D.: Application and methodology of dissolution dynamic nuclear polarization in physical, chemical and biological contexts, J. Magn. Reson., 305, 41–50, doi.org/10.1016/j.jmr.2019.06.001,

365 2019.

Krishna, M., English, S., Yamada, K., Yoo, J., Murugesan, R., Devasahayam, N., Cook, J. A., Golman, K., Ardenkjaer-Larsen, J. H., Subramanian, S., and Mitchell, J. B.: Overhauser enhanced magnetic resonance imaging for tumor oximetry: Co-registration of tumor anatomy and tissue oxygen concentration, Proc. Natl. Acad. Sci. U.S.A., 99, 2216–2221, doi.org/10.1073/pnas.042671399, 2002.

370   Krummenacker, J., Denysenkov, V., Terekhov, M., Schreiber, L., and Prisner, T. F.: DNP in MRI: An in-bore approach at 1,5 T, J. Magn. Reson., 215, 94-99, doi.org/10.1016/j.jmr.2011.12.015, 2012.

Kuo, P. H., Kanal, E., Abu-Alfa, A. K., and Cowper, S. E.: Gadolinium-based MR contrast agents and nephrogenic systemic fibrosis, Radiology, 242, 647– 649, doi.org/10.1148/radiol.2423061640, 2007.

Lilburn, D., Pavlovskaya, G., and Meersmann, T.: Perspectives of hyperpolarized noble gas MRI beyond ^{3}He, J. Magn.
375   Reson. 229, 173–186, doi.org/10.1016/j.jmr.2012.11.014, 2013.

Lingwood, M. D., Siaw, T. A., Sailasuta, N., Abulseoud, O. A., Chan, H. R., Ross, B. D., Bhattacharya, P., and Han, S.: Hyperpolarized water as an MR imaging contrast agent: feasibility of in vivo imaging in a rat model, Radiology, 265, 418– 425, doi.org/10.1148/radiol.12111804, 2012.

Lynch, W. B., Earle, K. A., and Freed, J. H.: 1-mm wave ESR spectrometer, Rev. Sci. Instrum., 59, 1345-1351,
380   doi.org/10.1063/1.1139720, 1988.

Mett, R., Sidabras, J., Anderson, J., Klug, C., and Hyde, J.: Rutile dielectric loop-gap resonator for X-band EPR spectroscopy of small aqueous samples, J. Magn. Reson., 307, 106585, doi.org/10.1016/j.jmr.2019.106585, 2019.

Milikisiyants, S., Nevzorov, A. A., and Smirnov, A. I.: Photonic band-gap resonators for high-field/high-frequency EPR of microliter-volume liquid aqueous samples, J. Magn. Reson., 296, 152–164,
385   doi.org/10.1016/j.jmr.2018.09.006, 2018.

Mishkovsky, M., Comment, A., and Gruetter, R.: In-vivo detection of brain Krebs cycle intermediate by hyperpolarized magnetic resonance, J. Cereb. Blood Flow & Metabol., 32, 2108-2113, doi.org/10.1038/jcbfm.2012.136, 2012.

Neugebauer, P. and Barra, A.-L.: New cavity design for broad-band quasi-optical HF-EPR spectroscopy, Appl. Magn. Reson., 37, 833–843, doi.org/10.1007/s00723-009-0092-5, 2010.

390   Neumann, M.: The dielectric constant of water - computer simulations with the MCY potential, J. Chem. Phys., 82, 5663– 5672, doi.org/10.1063/1.448553, 1985.

Olsson, L. E., Chai, C.-M., Axelsson, O., Karlsson, M., Golman, K., and Petersson, J. S.: MR coronary angiography in pigs with intraarterial injections of a hyperpolarized ^{13}C substance, Magn. Reson. Med., 55, 731–737, doi.org/10.1002/mrm.20847, 2006.

395   Perazella, M. A.: Current status of gadolinium toxicity in patients with kidney disease, Clin. J. Am. Soc. Nephrol., 4, 461– 469, doi.org/10.2215/CJN.06011108, 2009.

Pileio, G., Concistre, M., Carravetta, M., and Levitt, M.: Long-lived nuclear spin states in the solution NMR of four-spin systems, J. Magn. Reson., 182, 353-357, doi.org/10.1016/j.jmr.2006.06.034, 2006.

Poole, C. P. Jr.: Electron Spin Resonance: A Comprehensive Treatise on Experimental Techniques. Wiley, New York, 1967.

400   Prisner, T. F., Un, S., and Griffin, R. G.: Pulsed ESR at 140 GHz, Isr. J. Chem., 32, 357-363, doi.org/10.1002/IJCH.199200042, 1992.

Rinard, G. A. and Eaton, G. R.: Loop-Gap Resonators, in: L. J. Berliner (Ed.) Biological Magnetic Resonance, v. 24, Wiley, New York, 2005.

Salerno, M., Altes, T. A., Mugler, J. P., Nakatsu, M., Hatabu, H., and de Lange, E. E.: Hyperpolarized noble gas MR

405   imaging of the lung: potential clinical applications, Eur. J. Radiol., 40, 33-44, doi.org/10.1016/S0720-048X(01)00347-3, 2001.

Semelka, R. C., Ramalho, M., Al Obaidy, M., and Ramalho, J.: Gadolinium in Humans: A Family of Disorders, Am. J. Roentgenology, 207, 229-233, doi.org/10.2214/AJR.15.15842, 2016.

Smirnov, A. I. and Smirnova, T. I.: Resolving domains of interdigitated phospholipid membranes with 95 GHz spin labeling

410   EPR, Appl. Magn. Reson., 21, 453-467, doi.org/10.1007/BF03162420, 2001.

Thomsen, H. S., Is NSF only the tip of the "gadolinium toxicity" iceberg? J. Magn. Reson. Imag., 28, 284–286, doi.org/10.1002/jmri.21478, 2008

Topcuoglu, E., Topcuoglu, M., Oysu, M., and Bukte, M.: Does gadoterate meglumine cause gadolinium retention in the brain of children? A case–control study, J. Magn. Reson. Imag., 51, 1471-1477, doi.org/10.1002/jmri.26954, 2020.

415   van Tol, J., Brunel, L.-C., and Wylde, R. J.: A quasioptical transient electron spin resonance spectrometer operating at 120 and 240 GHz, Rev. Sci. Instrum., 76, 074101, doi.org/10.1063/1.1942533, 2005.

Westbrook, K., Caut-Roth, K., and Talbot, J.: MRI in practice, Wiley-Blackwell, Chichester, 2011.

420